Surface polarization, field homogeneity, and dielectric breakdown in ordered and disordered nanodielectrics based on gold-polystyrene superlattices

Roman Buchheit, Bart-Jan Niebuur, Lola González-García, Tobias Kraus**

Prof. Dr. Tobias Kraus
INM–Leibniz Institute for New Materials, Campus D2 2, 66123 Saarbrücken, Germany; Colloid and Interface Chemistry, Saarland University, Campus D2 2, 66123 Saarbrücken, Germany
Email Address: tobias.kraus@leibniz-inm.de
Dr. Lola González-García
INM–Leibniz Institute for New Materials, Campus D2 2, 66123 Saarbrücken, Germany; Department of Materials Science and Engineering, Saarland University, Campus D2 2, 66123 Saarbrücken, Germany
Email Address: lola.gonzalez-garcia@leibniz-inm.de
Dr.-Ing. Roman Buchheit, Dr. Bart-Jan Niebuur
INM–Leibniz Institute for New Materials, Campus D2 2, 66123 Saarbrücken, Germany

S1 Substrate surface profiles

The dielectric constants of hybrid layers were calculated assuming a parallel plate capacitor. To check the validity of this model, we compared the roughnesses of the substrates and the layers. We found smooth surfaces with arithmetic average surface roughness values, R_a, in the range of 0.8 nm to 1.0 nm, as measured over a surface area of 700 µm x 530 µm for the spin-coated samples. The surface profiles were numerically analyzed using the MetroPro software after subtraction of a plane (for the rigid spin-coated samples) or a cylinder (for the flexible inkjet printed sample) to obtain the roughness values listed in Table S1. Figure S1a and Figure S1b show representative surface profiles of the spin-coated dielectric samples. We measured both the surface roughness of the aluminium/silicon substrate ($R_a = 3.0$ nm, see Supporting Information of [1]) and of the aluminium/PET substrate ($R_a = 4.0$ nm, shown in Figure S1c) over an area of 100 µm x 100 µm with atomic force microscopy (AFM).

Table S1: Average surface roughness R_a of the hybrid dielectric layers (from white light interferometry) and of the aluminum electrode (from atomic force microscopy).

Sample label	coating method	R_a [nm]
$Au^{2.9\,nm}_{5\,vol\%}@PS_{5000}$	spin coated	0.8
$Au^{2.9\,nm}_{9\,vol\%}@PS_{11000}$	spin coated	0.8
$Au^{4.7\,nm}_{7\,vol\%}@PS_{5000}$	spin coated	1.0
$Au^{4.6\,nm}_{10\,vol\%}@PS_{11000}$	spin coated	1.0
$Au^{8.2\,nm}_{17\,vol\%}@PS_{5000}$	spin coated	1.1
$Au^{8.2\,nm}_{31\,vol\%}@PS_{11000}$	spin coated	1.0
$Au^{4.6\,nm}_{10\,vol\%}@PS_{11000}$	inkjet printed	110.9
Al coated PET foil	sputtered	4.0

Because the layer thickness of the spin-coated samples exceeded the roughness of the substrates and of the dielectric layers by one order of magnitude, the sample can be treated as a parallel plate capacitor,

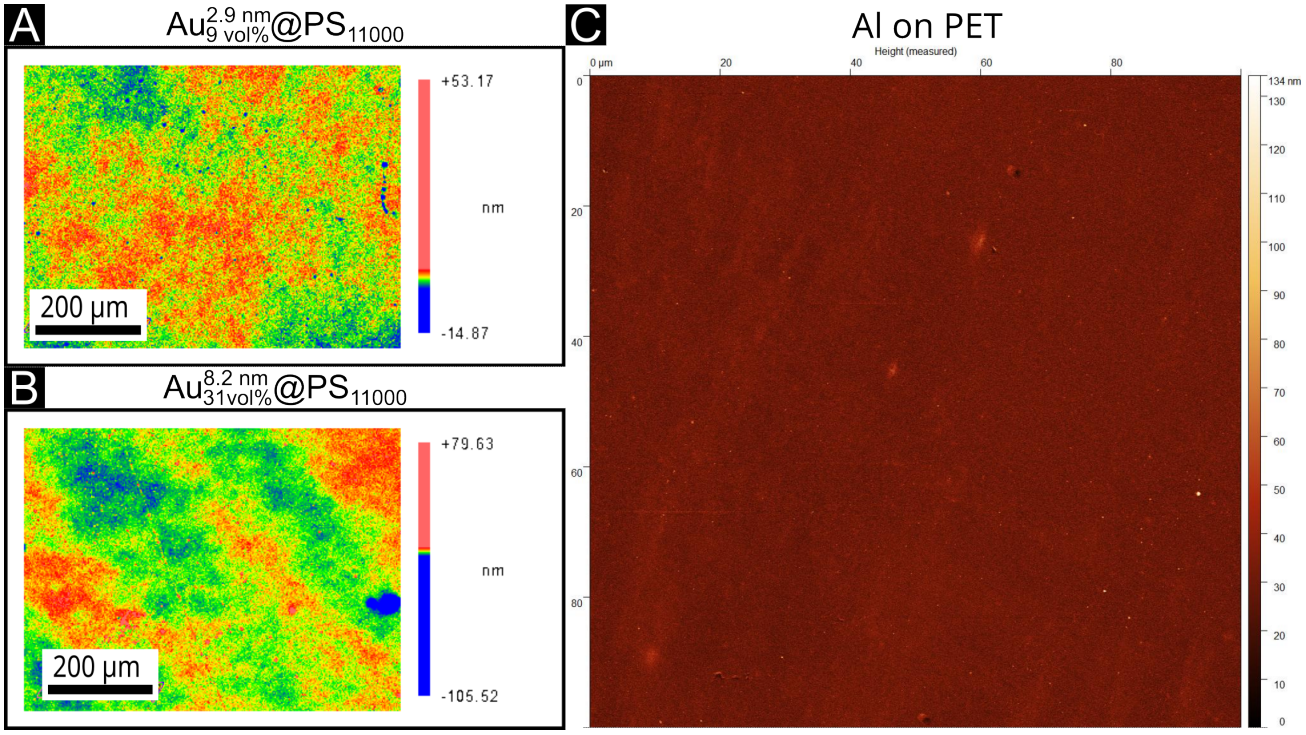

Figure S1: Surface profile measurements. Surface profiles measured with white light interferometry (WLI) of a) $Au^{2.9\,nm}_{9\,vol\%}@PS_{11000}$ and b) $Au^{8.2\,nm}_{31\,vol\%}@PS_{11000}$. c) Surface profile measured with atomic force microscopy of Al coated PET foil.

which allowed the determination of the dielectric constants. We found a much larger surface roughness of the inkjet printed sample; its effective thickness could only be estimated by the measured capacitance.

S2 Thermogravimetric analysis

We performed two thermogravimetric analysis (TGA) measurements for each prepared ink. Most of the mass loss occurred below $\approx$ 520 °C, therefore we assumed that that all residual mass at 520 °C was elemental gold; in further calculations, the mean values of the two measurements for each layer type that can be found in Figure S2 were used as the measured gold weight fraction $x_{w,Au}$.
We assumed compact films when calculating the fraction of Au in the dry Au@PS samples from the residual Au mass. The density of bulk Au ($\rho_{Au} = 19.32\,g\,cm^{-3}$ [2]) and the mean density of amorphous polystyrene ($\rho_{PS} = 1.05\,g\,cm^{-3}$ [3]) were used to calculate the volume fraction of Au $f_{v,Au}$:

$$f_{v,Au} = \frac{x_{w,Au}}{x_{w,Au} + \frac{\rho_{Au}}{\rho_{PS}}(1 - x_{w,Au})} \tag{S1}$$

Note that the assumption of a homogeneous polystyrene mass density is an approximation; it is possible that different ligand areal densities and ligand lengths or additional steps such as thermal annealing change the actual density of the polymer shells.
We assumed that all organic molecules in the layer were bound as ligand molecules and that the organic fraction was only made up by PS ligands when calculating the ligand density. The mass of the organic

shell per nanoparticle m_{organic} was calculated by

$$m_{\text{organic}} = m_{\text{AuNP}} \left(\frac{1}{x_{\text{w,Au}}} - 1 \right) = \rho_{\text{Au}} \frac{4}{3} \pi \left(\frac{d_{\text{core}}}{2} \right)^3 \left(\frac{1}{x_{\text{w,Au}}} - 1 \right) \tag{S2}$$

where m_{AuNP} is the mass of a single gold core, d_{core} the core diameter, ρ_{Au} the gold bulk density, and $x_{\text{w,Au}}$ the gold weight fraction. We calculated the number of PS ligands per nanoparticle n_{PS} using the molecular mass M_{PS} of the used PS ligand:

$$n_{\text{PS}} = m_{\text{organic}} / M_{\text{PS}} \tag{S3}$$

Finally, we obtained the ligand density $\rho_{\text{A,ligand}}$ by dividing the number of PS ligands per particle by the surface of the gold core A_{AuNP}:

$$\rho_{\text{A,ligand}} = \frac{n_{\text{PS}}}{A_{\text{AuNP}}} = \frac{n_{\text{PS}}}{4\pi \left(\frac{d_{\text{core}}}{2} \right)^2} \tag{S4}$$

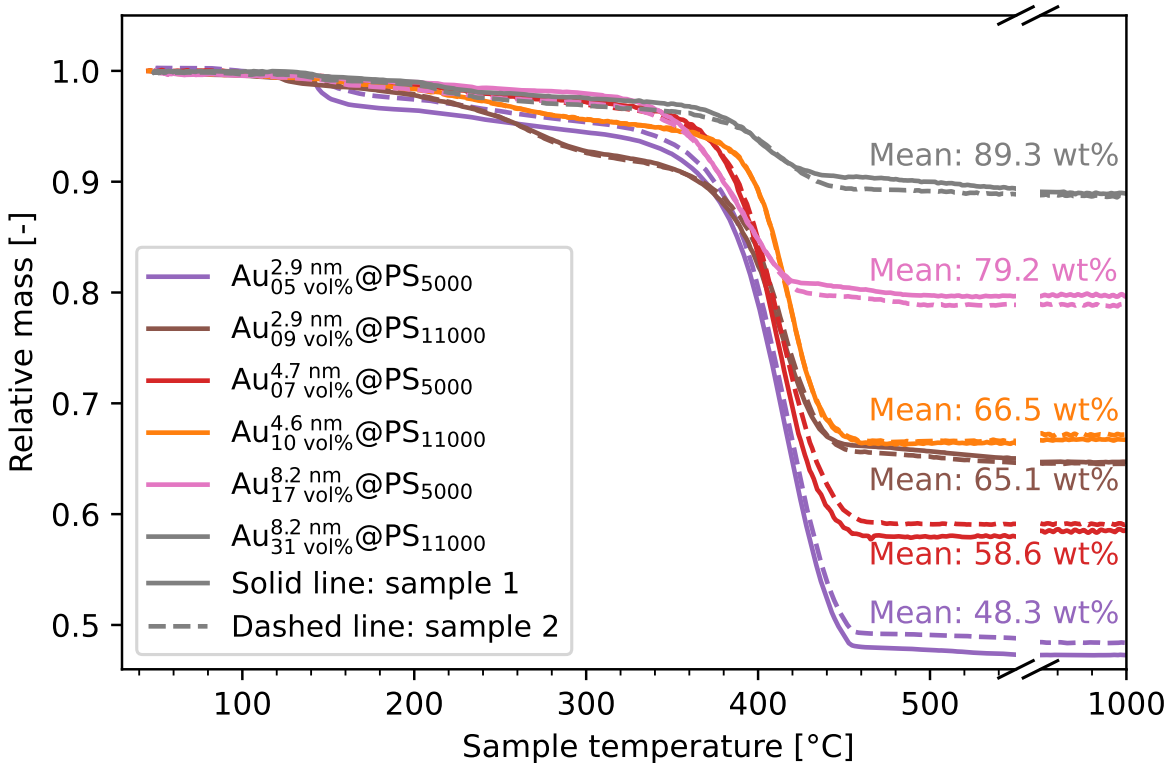

Figure S2: TGA results for all dielectric layers prepared with variation of Au core size and ligand length. The mean value of two measured samples is reported.

The resulting volume contents of gold in dried layers are listed in Table S2; additionally the Au concentrations in the inks as measured by UV-Vis spectroscopy are listed.

Table S2: Measured properties of the prepared Au@PS hybrid nanoparticle inks with varying Au core sizes and ligand length (dispersion medium toluene) with the diameter of the Au cores d_{core}, the Au volume fraction in dried layers $f_{\mathrm{v,Au}}$, the ligand density $\rho_{\mathrm{A,ligand}}$, and the Au concentration in the inks c_{Au}.

Ink label	d_{core} [nm]	Ligand	$\rho_{\mathrm{A,ligand}}$ [nm^{-2}]	$f_{\mathrm{v,Au}}$ [vol%]	c_{Au} [mg mL^{-1}]
$\mathrm{Au}^{2.9\,\mathrm{nm}}_{5\,\mathrm{vol\%}}@\mathrm{PS}_{5000}$	2.9	PS_{5000}	1.2	4.8	19.8
$\mathrm{Au}^{2.9\,\mathrm{nm}}_{9\,\mathrm{vol\%}}@\mathrm{PS}_{11000}$	2.9	PS_{11000}	0.3	9.2	24.7
$\mathrm{Au}^{4.7\,\mathrm{nm}}_{7\,\mathrm{vol\%}}@\mathrm{PS}_{5000}$	4.7	PS_{5000}	1.3	7.1	12.8
$\mathrm{Au}^{4.6\,\mathrm{nm}}_{10\,\mathrm{vol\%}}@\mathrm{PS}_{11000}$	4.6	PS_{11000}	0.4	9.7	34
$\mathrm{Au}^{8.2\,\mathrm{nm}}_{17\,\mathrm{vol\%}}@\mathrm{PS}_{5000}$	8.2	PS_{5000}	0.8	17.2	23
$\mathrm{Au}^{8.2\,\mathrm{nm}}_{31\,\mathrm{vol\%}}@\mathrm{PS}_{11000}$	8.2	PS_{11000}	0.2	31.2	26.4

S3 Characterization of the synthesized inks by SAXS, DLS, and TEM

The synthesis of the inks was performed in a two step process: First, oleylamine (OAm) capped AuNPs (Au@OAm NPs) were synthesized in different solvents. Then, the ligand exchange to thiol-terminated polystyrene was performed via stirring at 60 °C for one week (see Experimental Section of main paper for details) to obtain the final inks with toluene solvent. We performed small angle X-ray scattering (SAXS, see Figure S4 for small and large Au@PS particles and Supporting Information of our previous publication [1] for the SAXS patterns of the inks with medium-sized Au@PS particles) and dynamic light scattering (DLS) to characterize the inks. The SAXS measurements revealed the core diameters of the AuNPs d_{core} and the width of their distribution σ, the DLS measurements provided the hydrodynamic diameters d_{h} of the particles; the values for all nanoparticles derived from the scattering experiments are summarized in Table S3.

Table S3: Core size data with the mean and standard deviation of the core diameters d_{core} and σ from SAXS, and the hydrodynamic diameters d_{h} from DLS.

Sample name	d_{core} [nm]	σ [%]	d_{h} [nm]
small Au@OAm 1$^{\mathrm{st}}$ batch	2.9	8.5	6.5 ± 0.32
$\mathrm{Au}^{2.9\,\mathrm{nm}}_{5\,\mathrm{vol\%}}@\mathrm{PS}_{5000}$	2.9	9	12 ± 0.23
small Au@OAm 2$^{\mathrm{nd}}$ batch	2.9	10	6 ± 0.53
$\mathrm{Au}^{2.9\,\mathrm{nm}}_{9\,\mathrm{vol\%}}@\mathrm{PS}_{11000}$	2.9	12.9	11.2 ± 0.15
medium Au@OAm	4.7	6.7	7.7 ± 0.05
$\mathrm{Au}^{4.7\,\mathrm{nm}}_{7\,\mathrm{vol\%}}@\mathrm{PS}_{5000}$	4.7	7	16.3 ± 0.09
$\mathrm{Au}^{4.6\,\mathrm{nm}}_{10\,\mathrm{vol\%}}@\mathrm{PS}_{11000}$	4.6	6.6	16.2 ± 0.1
Large Au@OAm	7	10	N/A
Large Au@OAm 1x overgrow	8.2	8.5	11.2 ± 0.62
$\mathrm{Au}^{8.2\,\mathrm{nm}}_{17\,\mathrm{vol\%}}@\mathrm{PS}_{5000}$	8.2	9.3	20.3 ± 0.06
$\mathrm{Au}^{8.2\,\mathrm{nm}}_{31\,\mathrm{vol\%}}@\mathrm{PS}_{11000}$	8.2	9	19.4 ± 0.02

For $\mathrm{Au}^{\mathrm{small}}_{0.05}@\mathrm{PS}_{5000}$ and $\mathrm{Au}^{\mathrm{small}}_{0.09}@\mathrm{PS}_{11000}$, two batches of small oleylamine (OAm)-capped AuNPs (Au@OAm NPs) were synthesized (Figure S3a and Figure S3b) in n-pentane; for $\mathrm{Au}^{\mathrm{large}}_{0.17}@\mathrm{PS}_{5000}$ and $\mathrm{Au}^{\mathrm{large}}_{0.31}@\mathrm{PS}_{11000}$, one batch of Au@OAm NPs synthesized in benzene (Figure S3c) was overgrown to reach a final core diameter of 8.2 nm (Figure S3d). The TEM images indicate a narrowly dispersed size distribution of all the synthesized Au@OAm NPs. For $\mathrm{Au}^{4.7\,\mathrm{nm}}_{7\,\mathrm{vol\%}}@\mathrm{PS}_{5000}$ and $\mathrm{Au}^{4.6\,\mathrm{nm}}_{10\,\mathrm{vol\%}}@\mathrm{PS}_{11000}$ two batches of Au@OAm NPs were synthesized in n-hexane.

After ligand exchange, SAXS of the Au@PS nanoparticles in dispersion showed that the ligand exchange did not affect the Au cores for the 4.7 nm particles and 8.2 nm particles. The SAXS scattering pattern from the large particles fits very well to the form factor of spheres (Figure S4); there is no sign of agglomerates in the ink. The standard deviation σ was below 10 % and the monodispersity of the Au@PS particles is also seen on TEM images (Figure 1c in main paper). The same was found in our previous publication in SAXS measurements of the 4.7 nm Au@PS particles (see Supporting Information of [1]). Therefore, there is no sign that the ligand exchange affected the large and medium-sized Au cores. The hydrodynamic diameters increased for the 4.7 nm and 8.2 nm AuNPs during ligand exchange. The DLS data also show that there are no agglomerates in the inks composed of 4.7 nm and 8.2 nm particles.
For the liquid inks with 2.9 nm particles, especially $Au^{2.9\,nm}_{9\,vol\%}@PS_{11000}$, the SAXS data showed a deviation of the measured scattering data from a form factor of spheres. The observed deviation was, however, not connected to the presence of large agglomerates, as DLS data did not indicate agglomerates. For $Au^{2.9\,nm}_{5\,vol\%}@PS_{5000}$ the width of the core size distribution σ stays below 10 % and also the TEM image of the particles in Figure 1c in the main paper shows uniform particles. However, for $Au^{2.9\,nm}_{9\,vol\%}@PS_{11000}$ the width of the core size distribution was measured as $\sigma = 12.3\,\%$ (see Table S3). Therefore, we investigated the change of the $Au^{2.9\,nm}_{9\,vol\%}@PS_{11000}$ in more details by TEM. Figure S5 shows that during the ligand exchange at 60 °C, some AuNPs grew. We assume that Ostwald ripening was the origin of the appearance of larger AuNPs after the ligand exchange of $Au^{2.9\,nm}_{9\,vol\%}@PS_{11000}$. Two growth mechanisms, Ostwald ripening followed by coalescence of particles at longer ageing times, have been reported for alkanethiol-capped AuNPs in PMMA layers, which were annealed at 150 °C [5]. When comparing the ligand densities of all particles that were derived from TGA (see Table S2), we see that the ligand density for $Au^{2.9\,nm}_{9\,vol\%}@PS_{11000}$ with only 0.3 nm^{-2} is much lower than for $Au^{2.9\,nm}_{5\,vol\%}@PS_{5000}$. Consequently, it is proposed that the low ligand density of the $Au^{2.9\,nm}_{9\,vol\%}@PS_{11000}$ particles combined with a large curvature of the particles causing high surface energy could not protect the cores from degradation via Ostwald ripening during ligand exchange at 60 °C, while for all other inks, the polymer shells were dense enough to prevent degradation of the Au cores during ligand exchange.

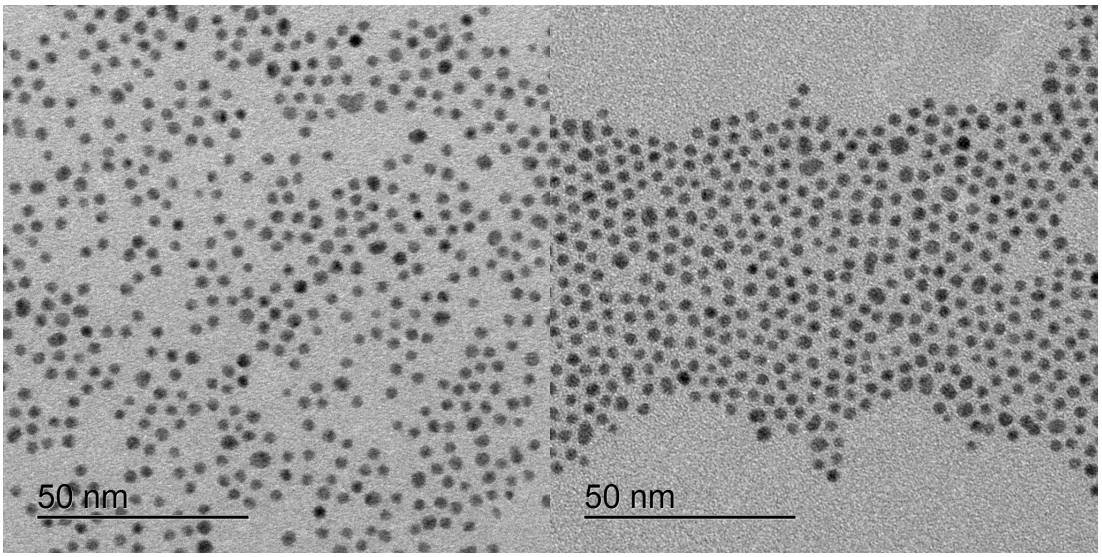

(a) Small Au@OAm NPs first batch. (b) Small Au@OAm NPs second batch.

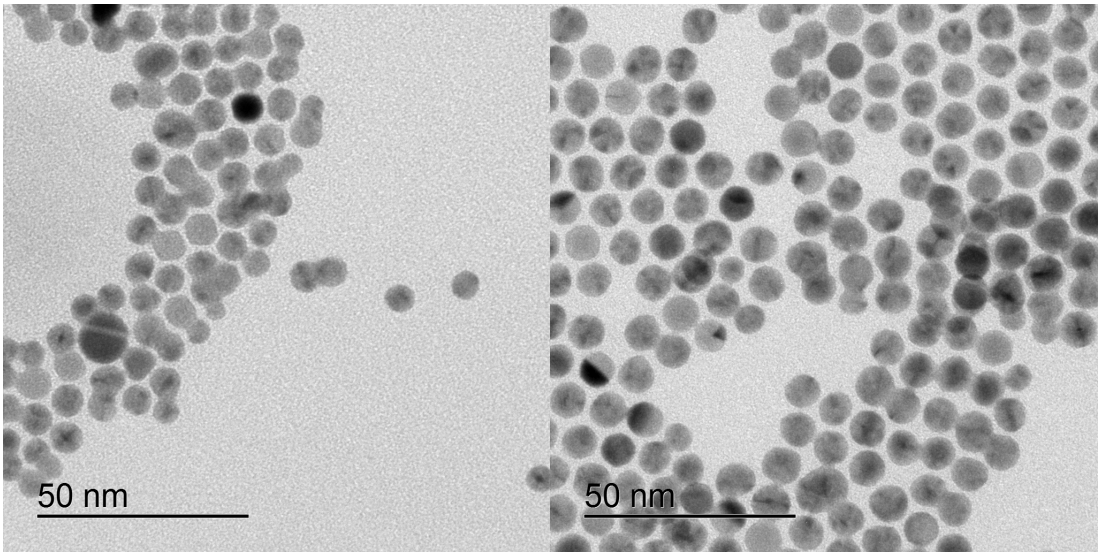

(c) Large Au@OAm NPs before overgrowth. (d) Large Au@OAm NPs after overgrowth.

Figure S3: TEM micrographs of synthesized Au@OAm NPs. a) The first batch of small Au@OAm NPs used for $Au_{0.05}^{small}@PS_{5000}$. b) The second batch of small Au@OAm NPs used for $Au_{0.09}^{small}@PS_{11000}$. c) The large Au@OAm NPs before overgrowth. d) The large Au@OAm NPs after overgrowth used for $Au_{0.17}^{large}@PS_{5000}$ and $Au_{0.31}^{large}@PS_{11000}$.

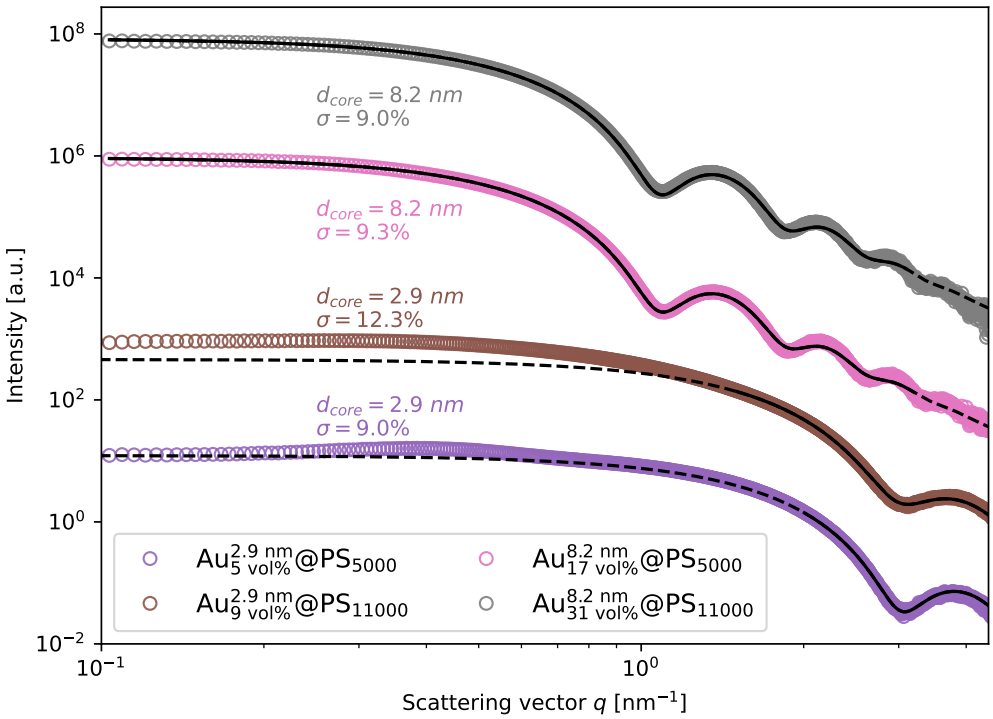

Figure S4: SAXS patterns of 2.9 nm Au@PS and 8.2 nm Au@PS particles dispersed in toluene after ligand exchange. The measurements were shifted in intensity by a multiplication factor. The black lines indicate fits using a form factor for spheres with diameters d_{core} and the widths of the core size distributions σ [4].

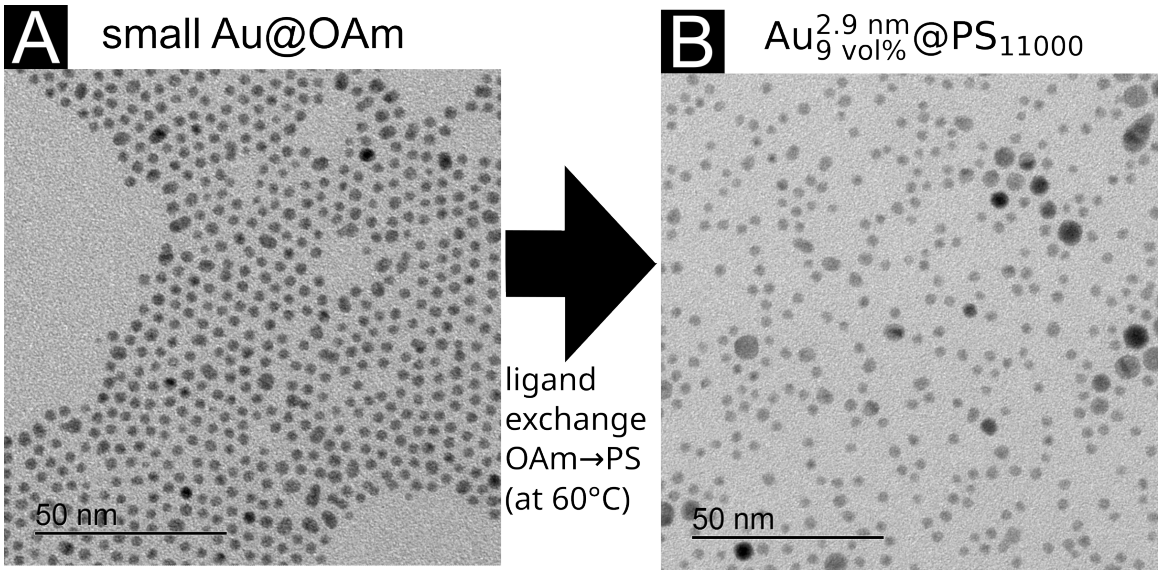

Figure S5: TEM images of a) small Au@OAm NPs and b) $Au^{2.9\,\mathrm{nm}}_{9\,\mathrm{vol\%}}@PS_{11000}$ after ligand exchange show the formation of large AuNPs in the ink.

S4 Packing structure of small and large particles

SAXS of dried drop casted films yielded the nature of particle packing and inter-particle distances. In our previous publication, we investigated the packing for 4.7 nm particles [1]. In this study, we measured the packing of drop-casted layers with 2.9 nm and 8.2 nm Au@PS particles. The SAXS patterns, acquired in transmission mode, are shown in Figure S6, the corresponding structure factors in Figure S7.
The center-to-center distance d_{cc} of the AuNPs in the drop casted samples follows from the position q^* of the primary structure factor peak, in a way depending on the underlying structure. In case of random packing this reads [6]:

$$d_{\mathrm{cc}}^{(rp)} = \frac{2\pi}{q^*} \tag{S5}$$

while for face-centered cubic (fcc) ordered particles

$$d_{\mathrm{cc}}^{(fcc)} = \frac{\sqrt{6}\pi}{q^*} \tag{S6}$$

is obtained. The particles' surface-to-surface distance d_{ss} follows in both cases as:

$$d_{\mathrm{ss}} = d_{\mathrm{cc}} - d_{\mathrm{core}}. \tag{S7}$$

The scattering curve obtained for $\mathrm{Au}_{5\,\mathrm{vol\%}}^{2.9\,\mathrm{nm}}\mathrm{@PS}_{5000}$ (Figure S6a) features a pronounced primary structure factor peak, q_1^*, at $0.97\,\mathrm{nm}^{-1}$, and a very weak secondary one at $\sim 2 \cdot q_1^*$. It can be concluded that the structure consist of randomly packed AuNPs with a surface-to-surface distance d_{cc} of 3.5 nm, calculated using Equations S5 and S7. This finding agrees with results obtained from TEM (Figure S8a), where also a random packing of AuNPs is observed.
$\mathrm{Au}_{9\,\mathrm{vol\%}}^{2.9\,\mathrm{nm}}\mathrm{@PS}_{11000}$ (Figure S6a) shows two structure factor peaks at $q_2^* \approx 1.12\,\mathrm{nm}^{-1}$ and $q_3^* \approx 1.51\,\mathrm{nm}^{-1}$. Because their relative positions do not match with classical crystalline structures, we conclude that these are two primary structure factor peaks, corresponding to two separate repeating structures at different length scales. The corresponding surface-to-surface distances, calculated assuming random packing for both separate structures, are 2.7 nm and 1.3 nm, respectively. As is shown by TEM (Figure S8b), the shell consisting of long PS-chains does not cover the AuNPs homogeneously, leading to multiple surface-to-surface distances. Furthermore, a very broad peak is visible at $q_1^* \approx 0.31\,\mathrm{nm}^{-1}$. It would correspond to a surface-to-surface distance of 17.6 nm, however such large spacings are not seen in the TEM (Figure S8b) and the exact origin of this peak is not completely clear to the authors.
The SAXS pattern of $\mathrm{Au}_{17\,\mathrm{vol\%}}^{8.2\,\mathrm{nm}}\mathrm{@PS}_{5000}$ is shown in Figure S6b. Also here, a series of structure factor peaks are visible. We identified a primary structure factor peak at $q_1^* = q_{111}^{\mathrm{fcc}} \approx 0.52\,\mathrm{nm}^{-1}$, and corresponding secondary peaks at $\sqrt{8/3} \cdot q_1^* = q_{200}^{\mathrm{fcc}}$, $\sqrt{11/3} \cdot q_1^* = q_{311}^{\mathrm{fcc}}$, $\sqrt{12/3} \cdot q_1^* = q_{222}^{\mathrm{fcc}}$, $\sqrt{19/3} \cdot q_1^* = q_{331}^{\mathrm{fcc}}$, $\sqrt{20/3} \cdot q_1^* = q_{420}^{\mathrm{fcc}}$ and $\sqrt{24/3} \cdot q_1^* = q_{422}^{\mathrm{fcc}}$ pointing to an fcc arrangement of the AuNPs [7]. Only the expected secondary peaks at $\sqrt{4/3} \cdot q_1^* = q_{200}^{\mathrm{fcc}}$ and $\sqrt{16/3} \cdot q_1^* = q_{400}^{\mathrm{fcc}}$ seem to be suppressed. According to Equations S6 and S7, the surface-to-surface distance equals 6.6 nm. The corresponding TEM image (Figure S8e) shows a weakly ordered structure, but an fcc arrangement is not discernible, which may be due to the small thickness of the sample measured by TEM.
The scattering pattern obtained for $\mathrm{Au}_{31\,\mathrm{vol\%}}^{8.2\,\mathrm{nm}}\mathrm{@PS}_{11000}$ (Figure S6b) is similar to that of $\mathrm{Au}_{9\,\mathrm{vol\%}}^{2.9\,\mathrm{nm}}\mathrm{@PS}_{11000}$. It has a relatively sharp primary structure factor at $q_2^* \approx 0.76\,\mathrm{nm}^{-1}$, indicating randomly packed AuNPs with a surface-to-surface distance of 0.1 nm. Due to the large size of the particles and the small ligand density, the van der Waals interaction is presumably strong enough to push aside the long PS ligands,

leading to the very close surface-to-surface distance. At $q_1^* \approx 0.39\,\mathrm{nm}^{-1}$, a second primary structure factor peak is observed, which may be attributed to very weakly ordered repeating structures with a repeat distance of $\approx$ 16 nm. These observations are in agreement with the results from TEM, shown in Figure S8f. The sample appears heterogeneous, with a few dense regions where AuNP cores almost touch, and more sparely populated regions.
In Table S4, an overview of all surface-to-surface distances is given.

Table S4: Experimental results for layers of Au@PS hybrid particles from SAXS. d_{core} is the Au core diameter, d_{ss}^1, d_{ss}^2, and d_{ss}^3 are characteristic surface-to-surface distances of the AuNPs in the dielectric layers. Distances without mark are calculated for random packing. Distances marked with $^{(\mathrm{fcc})}$ are calculated for fcc packing.

Sample name	d_{core} [nm]	d_{ss}^1 [nm]	d_{ss}^2 [nm]	d_{ss}^3 [nm]
$\mathrm{Au}^{2.9\,\mathrm{nm}}_{5\,\mathrm{vol\%}}@\mathrm{PS}_{5000}$	2.9	3.5	-	-
$\mathrm{Au}^{2.9\,\mathrm{nm}}_{9\,\mathrm{vol\%}}@\mathrm{PS}_{11000}$	2.9	17.6	2.7	1.3
$\mathrm{Au}^{4.7\,\mathrm{nm}}_{7\,\mathrm{vol\%}}@\mathrm{PS}_{5000}$	4.7	4.5	$2.5^{(\mathrm{fcc})}$	-
$\mathrm{Au}^{4.6\,\mathrm{nm}}_{10\,\mathrm{vol\%}}@\mathrm{PS}_{11000}$	4.6	6.2	0.7	-
$\mathrm{Au}^{8.2\,\mathrm{nm}}_{17\,\mathrm{vol\%}}@\mathrm{PS}_{5000}$	8.2	$6.6^{(\mathrm{fcc})}$	-	-
$\mathrm{Au}^{8.2\,\mathrm{nm}}_{31\,\mathrm{vol\%}}@\mathrm{PS}_{11000}$	8.2	8.0	0.1	-

Figure S8 shows TEM images of cross sections of thin film capacitors with dielectric layers for small Au cores with diameter of 2.9 nm, medium-sized cores with diameter of 4.7 nm, and large Au cores with diameter of 8.2 nm. The cross sections revealed that all packing types that were found in SAXS measurements of drop casted samples were also valid for spin-coated layers.

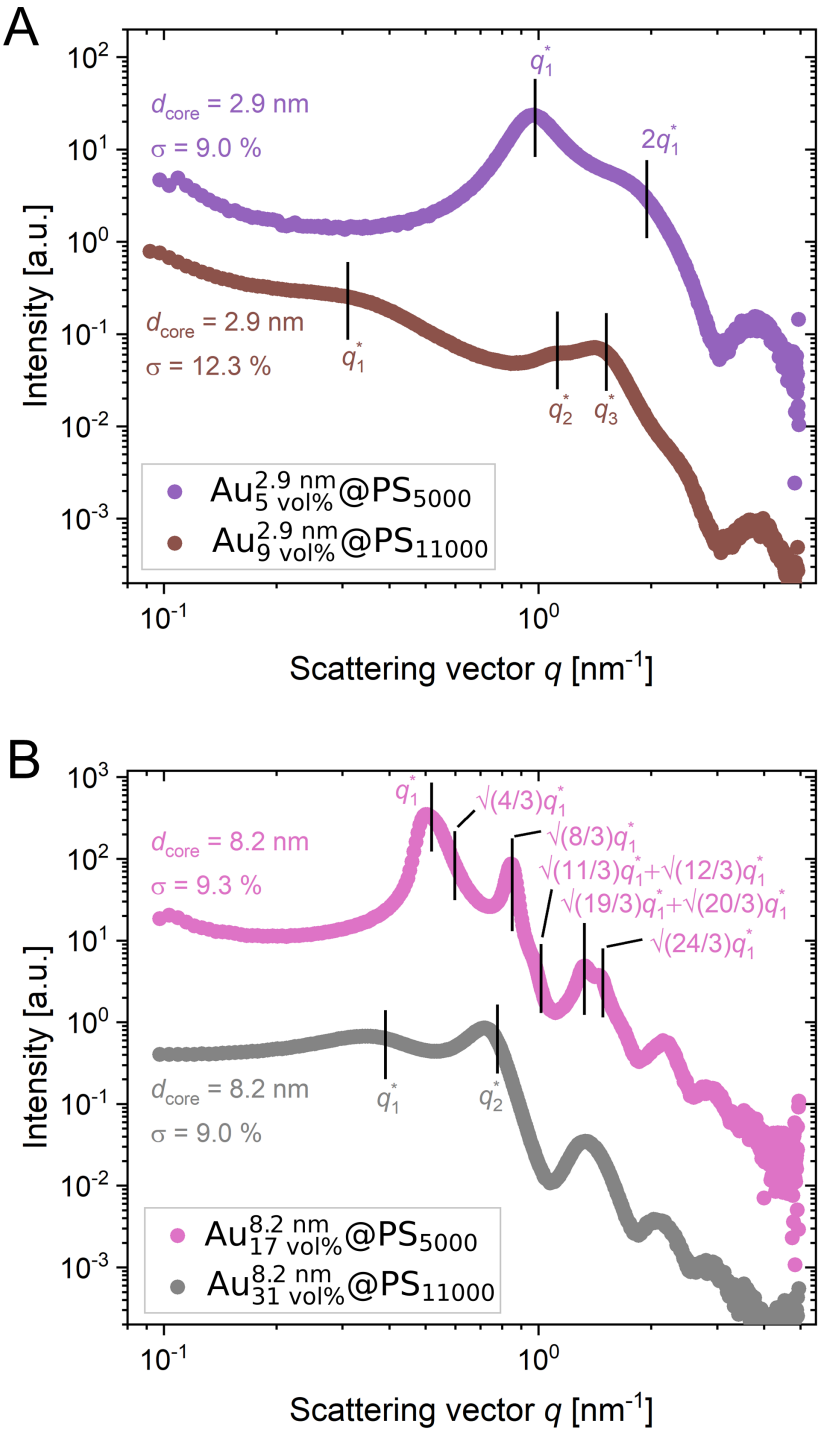

Figure S6: Transmission SAXS measurements of drop casted dielectric films on Kapton foil of Au@PS hybrid particles with a) small and b) large core sizes. The measurements were shifted in intensity by a multiplication factor.

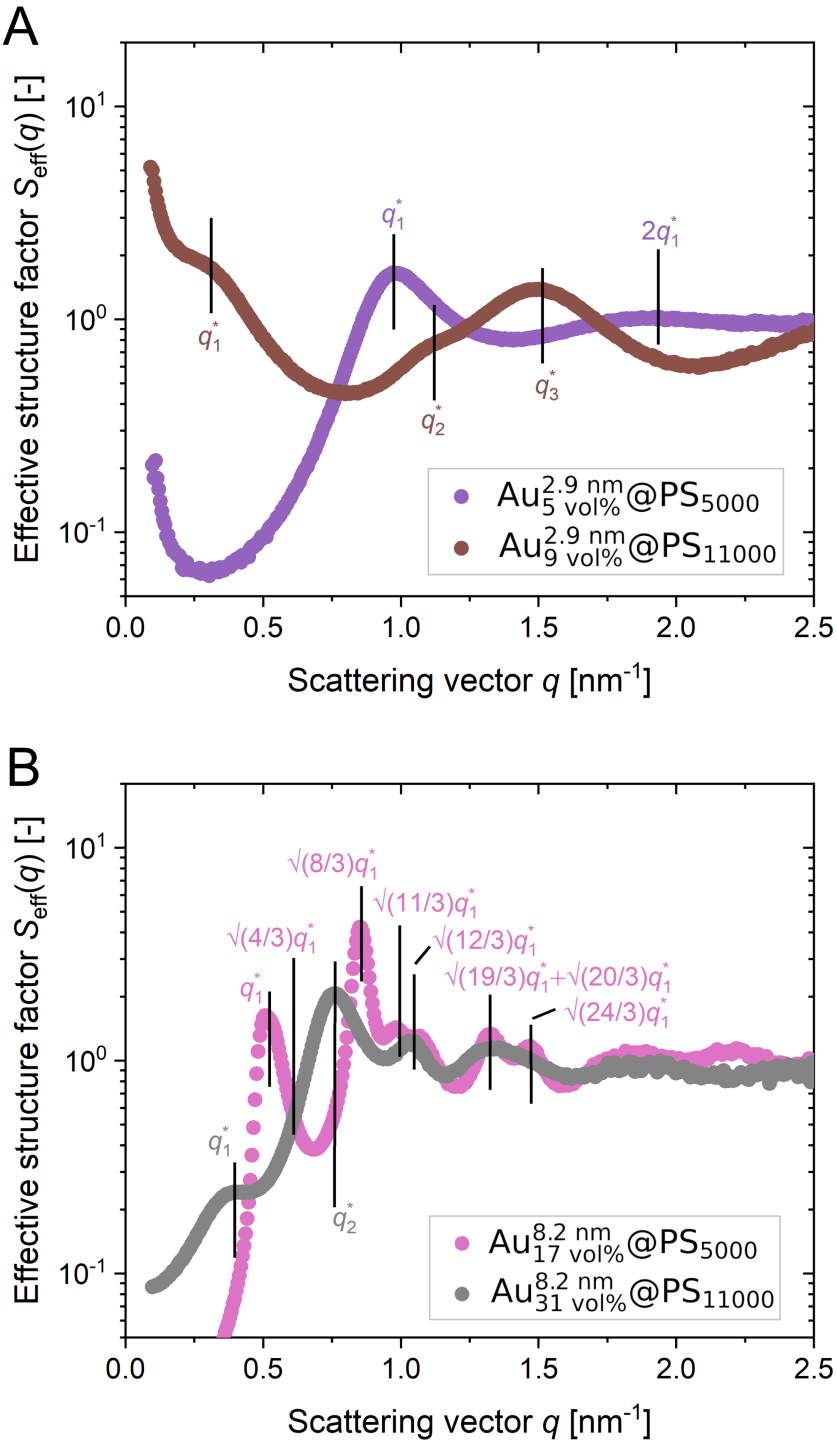

Figure S7: Effective structure factors $S_{\text{eff}}(q)$, determined by dividing the recorded transmission spectrum by the form factor of the particular nanoparticle in liquid dispersions, for the small and large Au@PS drop casted films measured in SAXS. While for $Au^{8.2\,\text{nm}}_{17\,\text{vol\%}}@PS_{5000}$ an fcc packing was found, for the other samples only a random packing was found.

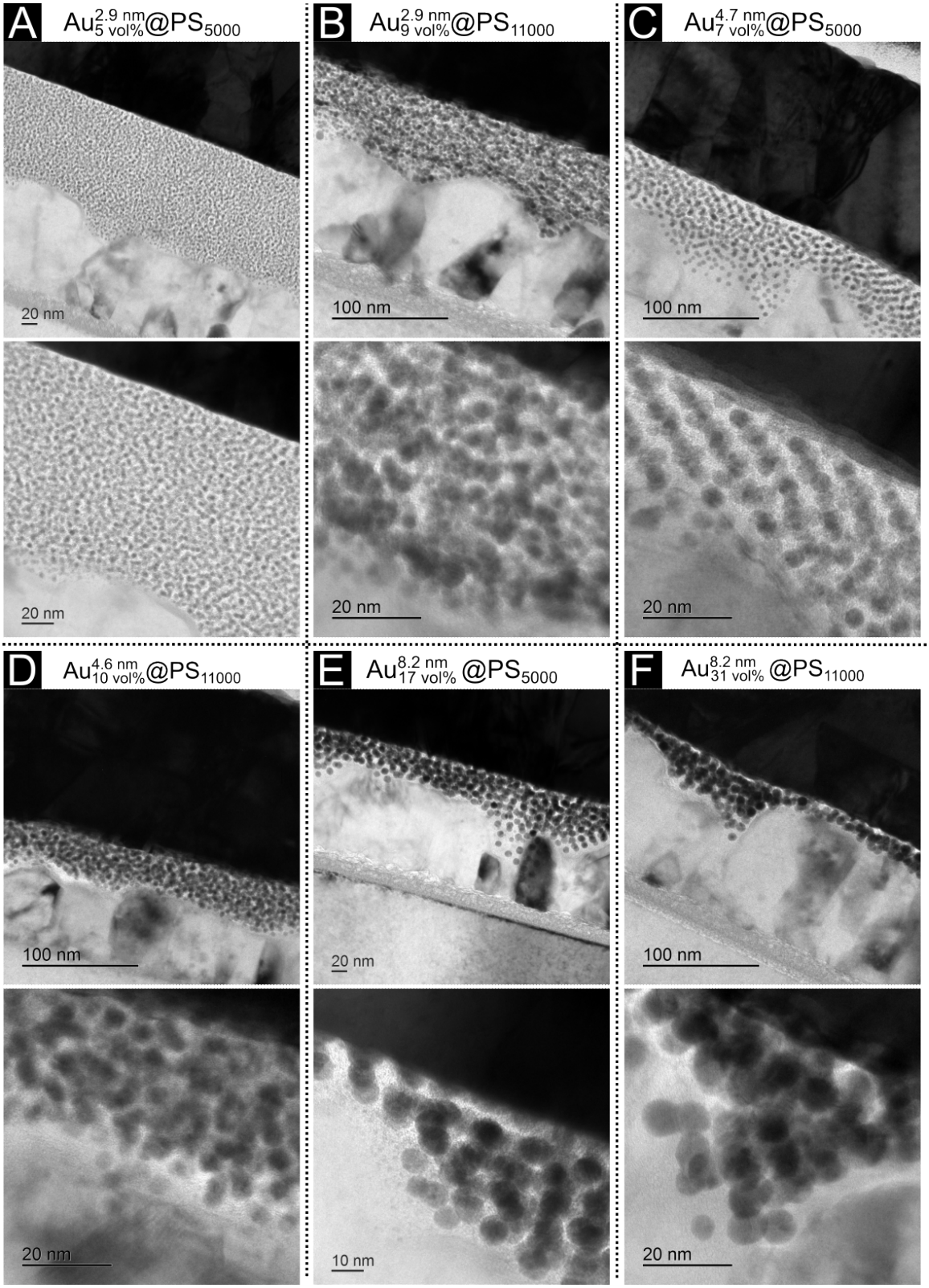

Figure S8: Transmission electron micrographs of focus ion beam cross sections of thin film capacitors with the a) $Au^{2.9\,nm}_{5\,vol\%}@PS_{5000}$, b) $Au^{2.9\,nm}_{9\,vol\%}@PS_{11000}$, c) $Au^{4.7\,nm}_{7\,vol\%}@PS_{5000}$, d) $Au^{4.6\,nm}_{10\,vol\%}@PS_{11000}$, e) $Au^{8.2\,nm}_{17\,vol\%}@PS_{5000}$, and f) $Au^{8.2\,nm}_{31\,vol\%}@PS_{11000}$ layers.

S5 Tabled data of thin film capacitors

Table S5: Overview of the dielectric constants ε_r at 10 kHz, the Au volume fractions f_v, and the specific interfacial areas $a_{s,interface}$ for Au@PS hybrids with different core sizes. Samples marked with * were shown as $Au_{0.05}^{disordered}$@PS and $Au_{0.21}^{disordered}$@PS in our previous publication [1].

Name	ε_r [−]	f_v [−]	$a_{s,interface}$ [$nm^2\,nm^{-3}$]
$Au_{5\,vol\%}^{2.9\,nm}@PS_{5000}$	3.2 ± 0.2	0.05	0.10
$Au_{9\,vol\%}^{2.9\,nm}@PS_{11000}$	6.7 ± 0.4	0.09	0.19
$Au_{7\,vol\%}^{4.7\,nm}@PS_{5000}$	3.4 ± 0.2	0.07	0.09
$Au_{10\,vol\%}^{4.6\,nm}@PS_{11000}$	4.8 ± 0.1	0.10	0.13
$Au@PS_{11000}$ ($d_{core} = 4.2\,nm$, $\rho_{A,ligand} = 0.7\,nm^{-2}$)*	3.1 ± 0.1	0.05	0.07
$Au@PS_{11000}$ ($d_{core} = 4.4\,nm$, $\rho_{A,ligand} = 0.2\,nm^{-2}$)*	34.3 ± 0.7	0.21	0.29
$Au_{17\,vol\%}^{8.2\,nm}@PS_{5000}$	4.9 ± 0.3	0.17	0.13
$Au_{31\,vol\%}^{8.2\,nm}@PS_{11000}$	13.6 ± 1.6	0.31	0.23

S6 Calculation of specific interfacial area

For the calculation of the specific interfacial area of the AuNP cores with the PS shells, the cores were assumed to be homogeneous spheres with a constant diameter. The interfacial area in the hybrid dielectric material of the thin film capacitor is calculated as

$$A_{interface} = N_{AuNP} A_{AuNP} = \frac{V_{Au}}{V_{AuNP}} A_{AuNP} = \frac{V_C f_{v,Au}}{V_{AuNP}} \tag{S8}$$

with N_{AuNP} the number of the AuNP, $A_{AuNP} = 4\pi(\frac{d_{core}}{2})^2$ the AuNP surface area, and V_{Au} the volume of the Au fraction

$$V_C = At \tag{S9}$$

where $A = 0.79\,mm^2$ is the area of the top contact and t the thickness of the respective dielectric layer. The resulting values from Equations S8 and S9 were used in Equation 2 in the main paper.

S7 Dielectric breakthrough

The dielectric breakdown was measured by applying an increasing voltage on thin film capacitors until an increase in the current was measured at the breakdown voltage V_{bd}. The measurements for 2.9 nm and 8.2 nm Au@PS particles are shown in Figure S9, the measurements for the 4.7 nm Au@PS particles were shown in the Supporting Information of [1].
We calculated the breakdown field strength E_{bd} with the equation

$$E_{bd} = \frac{V_{bd}}{t} \tag{S10}$$

where t is the thickness of the dielectric layer in the thin film capacitor. The resulting breakdown field strength are listed in Table S6.

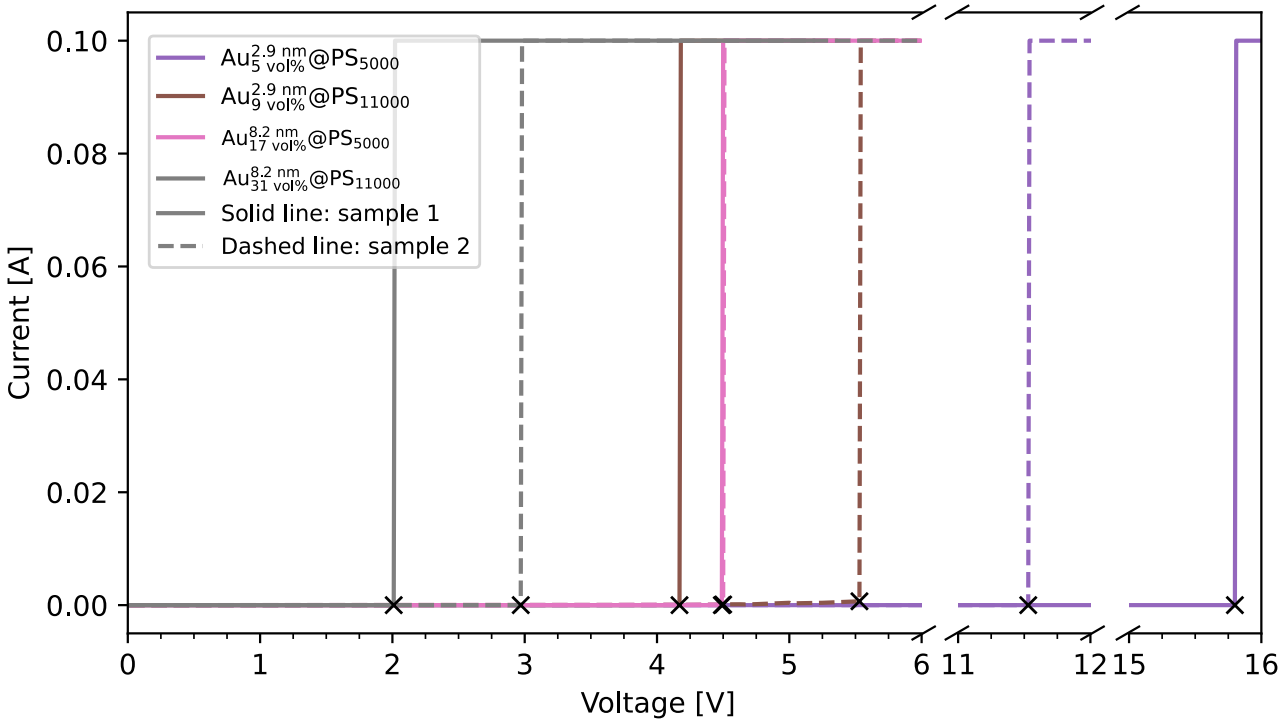

Figure S9: Dielectric breakthrough for dielectric layers with small and large gold cores.

Table S6: Estimated breakdown strengths E_{bd} of the dielectric films with Au cores of various sizes. The mean value of two measurements is reported.

Name of sample	E_{bd} [MV m^{-1}]
$Au^{2.9\,nm}_{5\,vol\%}$@PS_{5000}	100.9
$Au^{2.9\,nm}_{9\,vol\%}$@PS_{11000}	71.1
$Au^{4.7\,nm}_{7\,vol\%}$@PS_{5000}	154.3
$Au^{4.6\,nm}_{10\,vol\%}$@PS_{11000}	59.9
$Au^{8.2\,nm}_{17\,vol\%}$@PS_{5000}	158.7
$Au^{8.2\,nm}_{31\,vol\%}$@PS_{11000}	71.1

S8 Bending of inkjet printed samples

We bent the flexible thin film capacitor sample in a bending machine as shown in Figure S10b. After a set of 500 bending cycles, we removed the sample and measured the dielectric properties. The dielectric constant and the dielectric loss at 10 kHz and the yield of the functional thin film capacitors in dependence on the number of bending cycles is shown Figure S10a. We observed a drop of the capacitance at 10 kHz from 1.3 nF to 1.2 nF after the first 500 bending cycles, then the capacitance stayed constant until 3500 bending cycles. We see a plausible explanation in nanoparticle rearrangement and phase separation in these first bending cycles. Such densification of the particle packing was assumed for Au@PEDOT:PSS films, where an increase of conductivity was observed after bending of the films [8]. 20 % of the thin film capacitors failed after 2000 bending cycles but the yield then stayed constant. According SEM images, the capacitors did not fail in the dielectric layer (see Figure S11b,c). The sequential contacting and measuring of the samples caused damage on the Au top contacts (see Figure S11a) and could cause short circuits and failure. A detailed study of the failure mechanism would require more extensive statistical data, because the SEM images show only small sections of the bent sample.

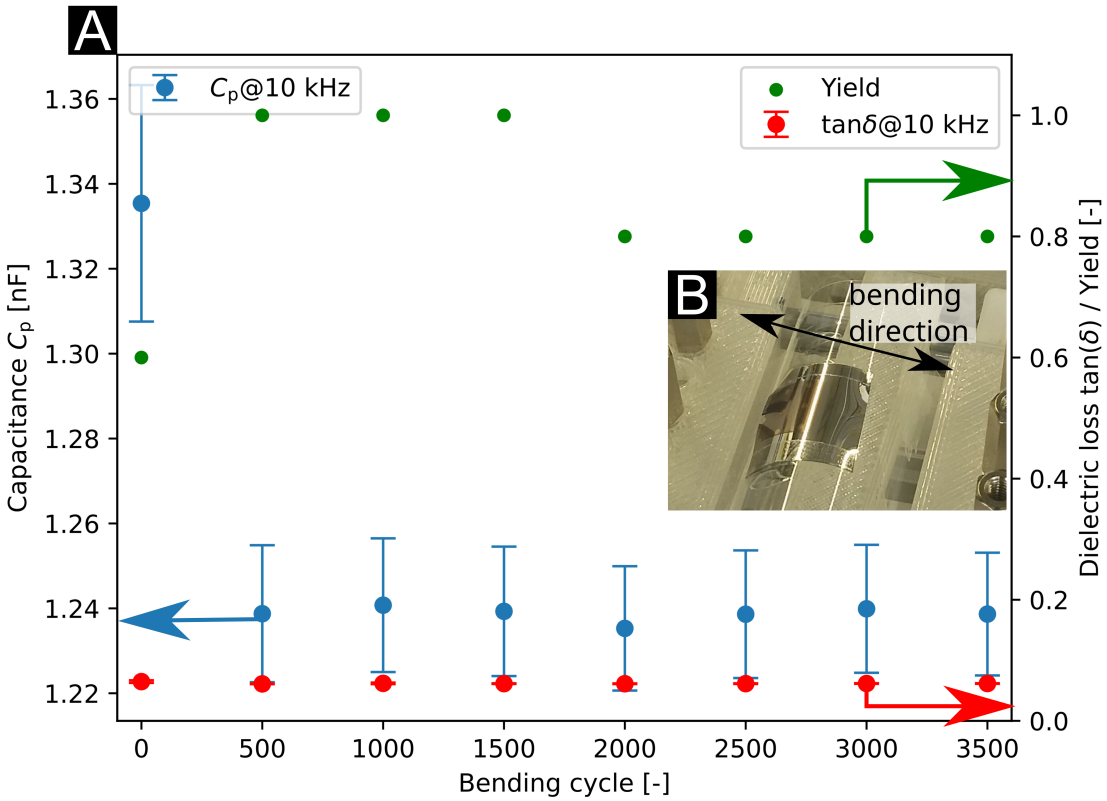

Figure S10: Bending study of flexible thin film capacitors on aluminium coated PET foil with inkjet printed $Au^{4.6\,nm}_{10\,vol\%}$@PS_{11000} dielectric layer. a) Dielectric constant, dielectric loss, and yield of functional thin film capacitors on the sample measured after sets of 500 bending cycles until up to 3500 bending cycles. b) The inset shows a photograph of the sample in the bending machine.

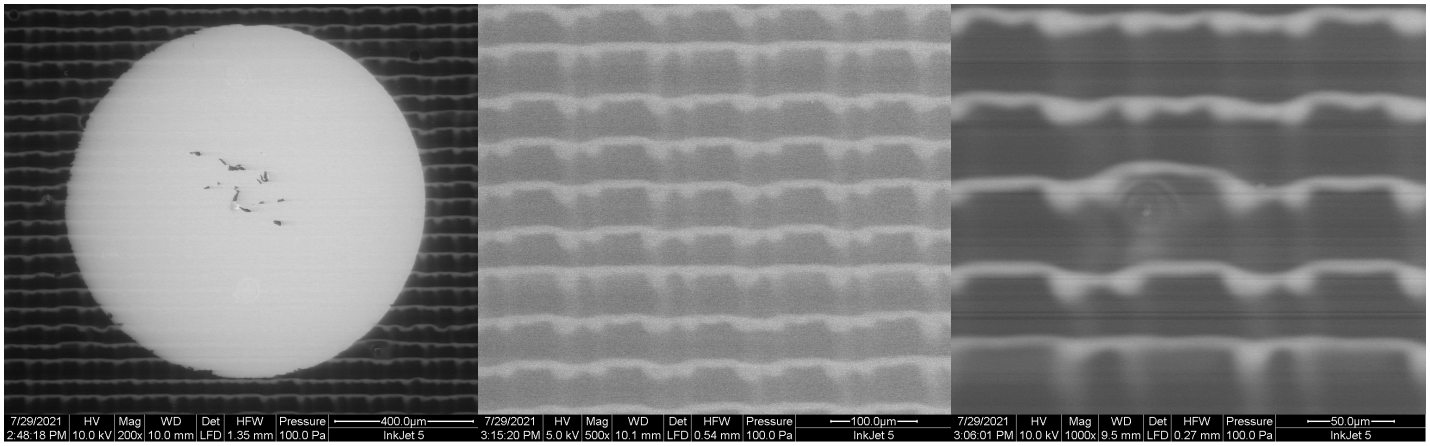

(a) (b) (c)

Figure S11: SEM micrographs of the inkjet printed $Au^{4.6\,nm}_{10\,vol\%}@PS_{11000}$ film after bending. a) The contacts showed damage from sequential contacting with the contact pins. b) Low magnification and c) high magnification micrographs of the film structure revealed no damage after bending.

References

[1] R. Buchheit, B. Kuttich, L. González-García, T. Kraus, *Advanced Materials* **2021**, *33*, 41 2103087.

[2] P. Atkins, J. de Paula, *Physical Chemistry*, Oxford University Press, New York, 9th edition edition, **2010**.

[3] J. Brandrup, editor, *Polymer handbook*, A Wiley-Interscience publication. Wiley, New York, NY, 4. ed. edition, **1999**.

[4] Rayleigh, *Proceedings of the Royal Society of London. Series A, Containing Papers of a Mathematical and Physical Character* **1914**, *90*, 619 324.

[5] L. Meli, P. F. Green, *ACS Nano* **2008**, *2*, 6 1305.

[6] T. Li, A. J. Senesi, B. Lee, *Chemical Reviews* **2016**, *116*, 18 11128.

[7] S. Förster, A. Timmann, M. Konrad, C. Schellbach, A. Meyer, S. S. Funari, P. Mulvaney, R. Knott, *The journal of physical chemistry. B* **2005**, *109*, 4 1347.

[8] A. Atashpendar, Dissertation, Albert-Ludwigs-Universität Freiburg, Freiburg, **11.02.2021**.